Dynamics of wind-forced coherent anticyclones in the open ocean

Inga Koszalka,[1] Annalisa Bracco,[2] James C. McWilliams,[3] and Antonello Provenzale[4]

[1]   We numerically study the dynamics of coherent anticyclonic eddies in the ocean interior. For the hydrostatic, rotating, stably stratified turbulence we use a high-resolution primitive equation model forced by small-scale winds in an idealized configuration. Many properties of the horizontal motions are found to be similar to those of two-dimensional and quasi-geostrophic turbulence. Major differences are a strong cyclone-anticyclone asymmetry linked to the straining field exerted by vortex Rossby waves, which is also found in shallow water flows, and the complex structure of the vertical velocity field, which we analyze in detail. Locally, the motion can become strongly ageostrophic, and vertical velocities associated with vortices can reach magnitudes and levels of spatial complexity akin to those reported for frontal regions. Transport and mixing properties of the flow field are further investigated by analyzing Lagrangian trajectories. Particles released in the pycnocline undergo large vertical excursions because of the vertical velocities associated to the vortices, with potentially important consequences for marine ecosystem dynamics.

1.   Introduction

[2]   Turbulence in the ocean encompasses many dynamical scales, from small three-dimensional swirls and eddies to the basin-scale circulation of global current systems. At the mesoscale, between about 10 and 500 km, ocean dynamics is often that of a stably stratified, rapidly rotating flow in the geostrophic, hydrostatic approximation. Mesoscale horizontal velocities are typically much larger than vertical velocities, and the motion is quasi-two-dimensional [*McWilliams et al.*, 1994]. This type of rotating flow is characterized by the presence of coherent vortices, long-lived concentrations of energy and vorticity [*McWilliams*, 1984, 1990] that densely populate many oceanic regions [*Stammer*, 1997].

[3]   Vortex dynamics in a stably stratified rotating flow has been investigated mainly in the frameworks of two-dimensional (2-D) and quasi-geostrophic (QG) turbulence [e.g., *Babiano et al.*, 1987; *McWilliams*, 1990; *Elhmaidi et al.*, 1993; *McWilliams et al.*, 1994; *Provenzale*, 1999; *Smith and Vallis*, 2001; *Bracco et al.*, 2004], neglecting the potentially complex structure of the vertical velocity field. Or it has been investigated in the framework of surface quasi-geostrophic (sQG) dynamics [*Held et al.*, 1995; *Constantin et al.*, 1999; *Lapeyre and Klein*, 2006] (where the velocity field is concentrated close to the surface) and

in shallow water (SW) flows [*Polvani et al.*, 1994; *Graves et al.*, 2006] (where the vertical velocity field is represented within a single vertical layer). Ocean dynamics and vertical velocities at mesoscales (10–500 km) and submesoscales (0.1–10 km) have been studied numerically in the context of primitive equation (PE) models, focusing on jet instability processes [*Levy et al.*, 2001; *Levy and Klein*, 2004] and large-scale simulations [*Klein et al.*, 2008], and in the context of nonhydrostatic models describing frontal areas [*Mahadevan and Tandon*, 2006]. Other works explored the use of the sQG equations to describe the vertical velocity field at the ocean surface [*LaCasce and Mahadevan*, 2006; *Lapeyre and Klein*, 2006] and of QG equations to analyze the role of mesoscale eddies [*Berloff et al.*, 2002; *Hogg et al.*, 2005; *Berloff et al.*, 2007]. Those studies suggest that near-mesoscale and submesoscale ocean dynamics can display many different facets, ranging from weakly sheared, vortex-dominated regions to intense frontal areas.

[4]   One question that remains open is the limits and the range of applicability of the results obtained with simpler 2-D and QG models of ocean mesoscale turbulence. To help fill this gap, in this work we use a high-resolution PE ocean model to study mesoscale turbulence in an idealized configuration that is the close to forced dissipated 2-D or SW turbulence. Here we do not include a mean flow or surface density anomalies, thus limiting the possibility of front formation. The configuration adopted is apt, even if extremely idealized, for describing the interior ocean dynamics of coherent vortices. In this configuration our results indicate that many properties of the horizontal flows in the PE setting are rather similar to those of 2-D, QG, and SW turbulence [e.g., *Polvani et al.*, 1994; *McWilliams et al.*, 1994; *Cho and Polvani*, 1996; *Bracco et al.*, 2004]. However, even in this idealized case we observe that the

[1]Institute of Geosciences, University of Oslo, Oslo, Norway.
[2]School of Earth and Atmospheric Science and Center for Nonlinear Science, Georgia Institute of Technology, Atlanta, Georgia, USA.
[3]Institute of Geophysics and Planetary Physics and Department of Atmospheric and Oceanic Sciences, University of California, Los Angeles, California, USA.
[4]ISAC, CNR, Turin, Italy.
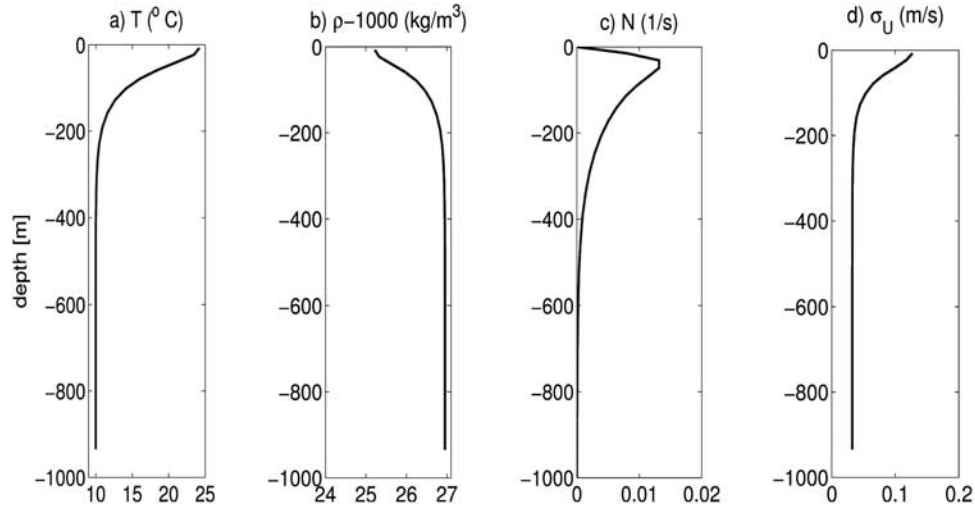
Figure 1. Twenty day averaged vertical profiles after stationarity has been reached. (a) Temperature, (b) density, (c) Brunt-Väisäla frequency in units of f, and (d) RMS of horizontal velocities.

vertical velocity distribution is spatially complex and not very consistent with its diagnostic characterization in QG dynamics. Indeed, vertical velocities cannot be easily parameterized, and ageostrophic effects are fundamental in determining the vertical transport properties of the vortices.

2. Numerical Model and Flow Description

[5] To integrate the system equations, we use the Regional Ocean Modeling System (ROMS), an incompressible, free surface, hydrostatic, primitive equation circulation model [*Shchepetkin and McWilliams*, 2005]. ROMS uses a generalized vertical, terrain-following coordinate system (s coordinate), where $s = \frac{z-\eta}{H+\eta}$, z being the height coordinate with $z = -H(x, y)$ representing the bottom of the model domain, and $\eta(x, y)$ describing the free surface elevation. In this coordinate system, even though the free surface can move, the computational domain is fixed ($1 \leq s \leq 0$).

[6] ROMS uses a third-order upstream-biased advection scheme in the horizontal [*Shchepetkin and McWilliams*, 1998], and a fourth-order centered scheme in the vertical. The nondimensional quadratic bottom drag parameter is 3×10^{-4}. Biharmonic horizontal diffusion acts along s surfaces with a coefficient $A_H = 10^6$ m^4 s^{-1} for all fields. Vertical mixing is parameterized by a nonlocal K profile (KPP) scheme [*Large et al.*, 1994]. The KPP parameterization is used to treat unresolved processes involved in ocean vertical mixing and considers distinct mixing processes in the interior and in the surface boundary layer. In particular, in the interior mixing is modeled as function of the local gradient Richardson number to represent shear instability of internal wave activity and of double diffusion. In the boundary layer mixing is enhanced because of the influence of surface forcing and is represented through a polynomial profile. The boundary layer profile agrees with similarity theory of turbulence and is matched, in the asymptotic sense, to the interior. The boundary layer depth is determined at each grid point.

[7] For consistency with previous works on 2-D and QG turbulence we adopt a doubly periodic configuration. We assume a constant depth $H = 1000$ m and lateral size $L = $ 256 km. We use a resolution $\Delta x = 1$ km in the horizontal and 20 layers in the vertical, 7 of which are confined in the upper 100 m of the water column. The Coriolis frequency is $f = 10^{-4}$ s^{-1}. The flow is initially at rest, and it is forced by a wind forcing that is used as an artifice to maintain mesoscale turbulence in a homogeneous domain in lieu of the inclusion of inhomogeneous mean flow instability processes, which are the primary mesoscale source in the real ocean. Here the wind forcing has a narrow-band continuous spectrum centered on the wave number $k_x = k_y = 6$ (about 40 km), i.e., with a radial wave number $k_f = \sqrt{k_x^2 + k_y^2} \sim 8$. Different realizations with identical power spectra are linearly interpolated every 20 days. This forcing is a close approximation to that adopted in simulations of forced 2-D or QG turbulence [*Elhmaidi et al.*, 1993; *Babiano and Provenzale*, 2007], and it implies weak surface buoyancy gradients. As a result, vorticity distribution in the flow resembles that of quasigeostrophic solutions and is less frontal than found in other recent idealized studies focused on surface frontal ocean dynamics [*Mahadevan and Tandon*, 2006; *Capet et al.*, 2008b, 2008c; *Klein et al.*, 2008] where sQG provides a better approximation [*Capet et al.*, 2008a; M. J. Molemaker et al., Balanced and unbalanced routes to dissipation in an equilibrated Eady flow, submitted to *Journal of Fluid Mechanics*, 2009].

[8] To forestall energy accumulation and flow barotropization [*Smith and Vallis*, 2001], we impose a relaxation, with a time constant of 60 days, to fixed temperature and salinity profiles obtained by fitting extratropical oceanic samples [*Conkright et al.*, 2002]. These profiles are uniform in the first 20 m of the water column (to simulate the presence of a surface mixed layer) and decay exponentially below the mixed layer (Figure 1). The relaxation to fixed temperature and salinity profiles is another artifice in lieu of the inhomogeneous eddy dispersal processes in the real ocean.

[9] We also analyzed a series of runs with a more idealized sinusoidal wind stress centered on the same wave number, i.e., $\tau^x(x, y) = 0.1[\sin(2\pi k_x x/L)\sin(2\pi k_y y/L) + 0.3 \, d\xi]$ N m^{-2}, where $d\xi$ is a random white noise component

added at each time step. In this further simplified configuration we investigated the role of vertical resolution by performing three simulations, one with 20 layers as in the case above and two with 80 layers, of which 22 layers were confined in the first 100 m; the simulations were run with and without a mixed layer in the upper 20 m. We briefly discuss the vertical resolution dependence and the impact of a mixed layer in section 4.

[10] After an initial transient of about 200 days the system reaches statistical stationarity. The characteristic root mean square horizontal and vertical velocities of the flow are $U \approx 0.1 \text{ m s}^{-1}$ and $W \approx 1.0 \times 10^{-4} \text{ m s}^{-1}$, respectively. Vertical profiles of temperature, density, and Brunt-Väisälä frequency, averaged over 20 days after the stationary state has been reached are shown in Figure 1. The motion is mainly horizontal; it is surface intensified in the upper $120-150$ m and captured by the first baroclinic mode. Most of the vortices are indeed confined in this upper region approximately between the surface and the 1026.7 kg m^{-3} isopycnal. The first internal radius of deformation within this region can be calculated as $L_d = \sqrt{(g'H/f)} \approx 15$ km, with H the depth of this surface layer. The internal Rossby radius of deformation L_d is small compared to the domain size, and the average Rossby number is $Ro = \frac{U}{fL_t} \approx 0.06$, where $L_t \approx L_d$ is the typical size of a vortex. The local value of Ro, especially in the cores of coherent vortices and in the upper 150 m of the water column, can be much larger than the average, as estimated by the value of ζ/f (seen in Figures 2a–2c) leading to strongly ageostrophic motion. Divergence is about 1 order of magnitude smaller than relative vorticity, and its spatial distribution is determined by vortices and filaments.

[11] The flow is dominated by intense anticyclones while most cyclones are short-lived and are destroyed after a few turnover times, usually leaving rings of positive vorticity around the anticyclones (Figure 2a). The dominance of anticyclonic vortices is evident also in the relative vorticity probability density functions (pdf's) shown in Figure 2d for various vertical levels. Long, negative tails characterize the vorticity pdf's that have all kurtosis larger than 7 and skewness between -1.75 and -6. The greatest values in both kurtosis and skewness are attained at depths between 75 and 150 m. The preferential existence of anticyclonic vortices in flows with small L_d and finite Ro has been found in idealized SW studies [*Cushman-Roisin and Tang*, 1990; *Arai and Yamagata*, 1994; *Polvani et al.*, 1994; *Cho and Polvani*, 1996] and in fully three-dimensional flows [*Yavneh et al.*, 1997]. *Graves et al.* [2006] demonstrated with a weakly nonlinear shallow water model that the disparity in the number of cyclones versus anticyclones results from a stronger weakening of cyclones under strain-induced deformation and a subsequent reaxisymmetrization of the vortex by vortex Rossby waves (VRWs), whose presence is evident in Figure 2e. Axisymmetry guarantees that a vortex is a stationary and linearly stable solution of the momentum equations in gradient wind and hydrostatic balance. If perturbed by an external strain field, a vortex monopole will relax back to an axisymmetric state on an advective time scale. As shown by *Montgomery and Kallenbach* [1997] and *Graves et al.* [2006], the relaxation process toward the axisymmetric shape includes the development of shielding rings of vorticity, or VRWs, that propagate

outward while being azimuthally sheared by the differential angular velocity of the vortex. *Graves et al.* [2006] have shown that whenever L_d is small and Ro is finite, as in our numerical simulations, strain-induced VRWs on the periphery of the vortices weaken cyclones far more strongly than anticyclones. Anticyclones can even strengthen systematically whenever the deformation radius is comparable to the vortex radius, with the VRWs transferring their energy back to the vortex.

## 3. Properties of the Horizontal Flow

[12] In this section we briefly discuss the horizontal transport and mixing properties of the simulated flow field.

[13] Figure 3a shows the horizontal kinetic energy spectra at depths of 5, 20, 78 and 204 m. In the upper 100 m, the spectra for $k > k_f$ are slightly steeper than k^{-3}, consistent with the behavior of two-dimensional turbulence in the direct enstrophy cascade [e.g., *Elhmaidi et al.*, 1993; *Babiano and Provenzale*, 2007], with simulations of shallow water turbulence [*Cho and Polvani*, 1996], and with forced dissipated homogeneous stratified quasi-geostrophic turbulence [*Smith and Vallis*, 2002]. Since L_d is comparable to the forcing scale, an inverse energy cascade is not present. (We verified that the spectra slopes do not change significantly but remain steeper than k^{-3} doubling the horizontal resolution on a smaller domain).

[14] Probability density functions (pdf's) of horizontal velocities are an important ingredient for modeling particle dispersion processes [*Pasquero et al.*, 2001]. In the vigorous upper layers we observe velocity pdf's that deviate from a Gaussian distribution (Figure 3b). This behavior is analogous to what is obtained from theoretical and numerical studies of vortex-dominated 2-D turbulence and point vortex systems [*Bracco et al.*, 2000a], sQG flows [*Schorghofer*, 2000], as well as oceanographic observations in regions of strong mesoscale activity [*Bracco et al.*, 2000b; *LaCasce*, 2005; *Isern-Fontanet et al.*, 2006]. Following those studies, we can pinpoint the source of non-Gaussianity and look at the velocity pdf's inside and outside vortices. We identify vortices as connected regions where the Okubo-Weiss parameter $OW = S^2 - \zeta^2$ is such that $OW < -\sigma_O W$, where S^2 is squared strain, ζ is vorticity, and $\sigma_O W$ is the standard deviation of OW [*Weiss*, 1981]. As shown by *Petersen et al.* [2006], OW in 2-D and QG flows is equal, apart from a constant factor, to the middle eigenvalue of a tensor of velocity gradients. The same eigenvalue is used to identify coherent structures in 3-D turbulent flows. Here, given the different set of equations considered (PE instead of QG or 2-D) OW represents an approximation of the middle eigenvalue of the velocity gradient tensor. However, it still provides a clear-cut separation between vorticity-dominated regions where $OW \ll 0$ and strain-dominated regions where $OW \gg 0$ whenever divergence is small, as in our case. Inside vortices, pdf's of horizontal velocity are nearly Gaussian, while in the background flow between vortices the pdf's are almost identical to those calculated for the whole domain, with long non-Gaussian tails. In vortex-dominated flows, non-Gaussian distributions in the background are nonlocally generated by the far-field velocity induced by the vortices [*Bracco et al.*, 2000a]. At lower layers, where the kinetic energy is much smaller and
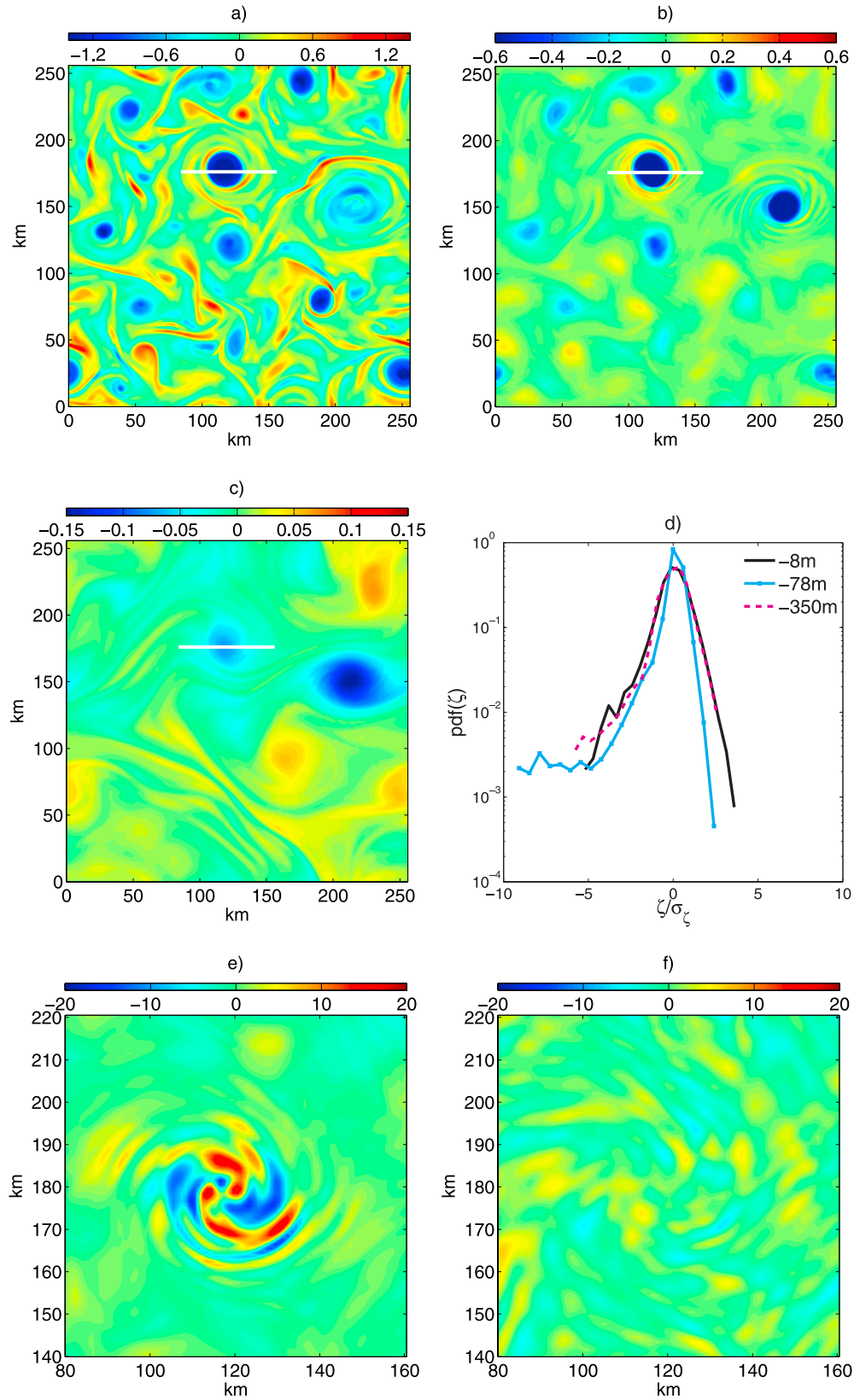
Figure 2. Vertical component of (nondimensional) relative vorticity ζ/f (a) at the surface (values between -1.2 and 1.2), (b) at 78 m depth (values between -0.6 and 0.6), and (c) at 350 m depth (values between -0.15 and 0.15). The nondimensional vorticity ζ/f provides an estimate of the local value of the Rossby number. (d) Normalized pdf's of relative vorticity at 8 (near the surface), at 78, and at 350 m. Vertical velocity in m d^{-1} (e) at 78 and (f) at 350 m depth in and around the vortex centered (120 km, 180 km). All fields are averaged over 1 day, thus removing near-inertial motion.
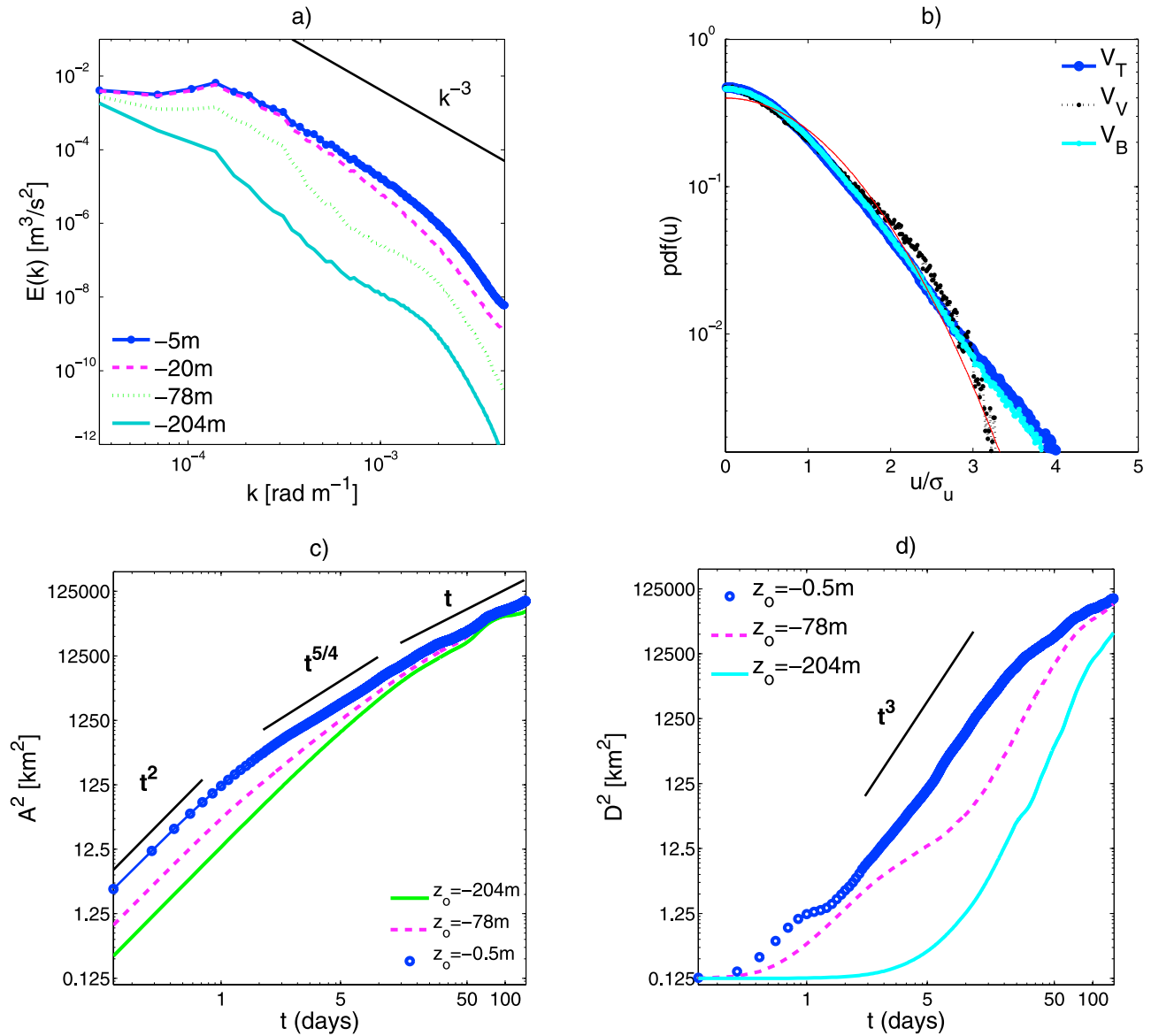
Figure 3. (a) Power spectra of horizontal kinetic energy at 5, 20, 78, and 204 m depth. (b) The pdf's of normalized horizontal velocities at 5 m depth over the entire domain (V_T), inside vortex cores (V_V), and in the background turbulence between the vortices (V_B). A Gaussian distribution (thin solid line) is shown for comparison. (c) Absolute dispersion of Lagrangian particles at 0.5 (black circles), 78 (gray dashed line), and 204 m (gray solid line). (d) Relative dispersion of couples of Lagrangian particles, same release depths as in Figure 3c.

vortices are either absent or weak, the velocity pdf's become approximately Gaussian (not shown). In QG turbulence, vortices and filaments determine the transport and mixing properties [*Provenzale*, 1999; *Bracco et al.*, 2004]. To investigate if this conclusion carries over to a more realistic flow, we deploy three sets of 4096 pairs of neutral Lagrangian particles uniformly distributed over the domain at initial depths 0.5, 78, and 204 m once stationarity has been reached. The particles are then passively carried by the 3-D Eulerian velocity field for 150 days. A first measure of transport properties is provided by horizontal absolute dispersion; it describes the time evolution of the mean horizontal square distance traveled by each particle, and it is defined as $A^2(t_0; t) = \langle |\mathbf{X}_i(t) - \mathbf{X}_i(t_0)|^2 \rangle$, where angular

brackets indicate average over all the particles released at a given vertical level at t_0. $\mathbf{X}_i(t)$ is the (x, y) position of the ith particle at time t (Figure 3c). Close to the surface, the dispersion curve shows both ballistic ($A^2 \sim t^2$) and Brownian ($A^2 \sim t$) regimes, respectively, for short ($t < 0.5$ day) and long ($t > 30$ days) times. An anomalous dispersion regime $A^2 \sim t^{5/4}$ appears at intermediate times, as observed in vortex-dominated barotropic and QG turbulence [*Elhmaidi et al.*, 1993; *Bracco et al.*, 2004]. The anomalous regime is absent at greater depths, where the vortices do not extend their influence. Mixing properties are quantified by relative dispersion, $D^2(t_0; t) = \langle |\mathbf{X} - \mathbf{X}'|^2 \rangle$, which describes the time evolution of the average separation of particle pairs. Here $\mathbf{X}$ and $\mathbf{X}'$ are the positions of two initially nearby particles, and

the brackets indicate average over all independent pairs. For 2-D turbulence, classical dispersion theories predict $D^2(t) \sim t^3$ when the separation is in the energy cascade range [*Richardson*, 1926]. Figure 3d shows relative dispersion computed at different depths: all three curves display an intermediate Richardson regime and converge at late times to a diffusive regime, as in numerical simulations of 2-D barotropic and QG flows [*Babiano et al.*, 1990; *Bracco et al.*, 2004]. Power laws with exponents between 2 and 3 have also been reported for relative dispersion of surface ocean drifters [*LaCasce and Ohlmann*, 2003].

[15] Analogous results are obtained for simulations without a surface mixed layer, for the runs forced with the idealized sinusoidal wind stress independent of vertical resolution, and for freely decaying simulations where the wind and solar forcing are turned off. Overall, we can conclude that many properties of horizontal motions in the upper layer of a stably stratified, hydrostatic, rapidly rotating PE flow in the configuration considered here are similar to those of 2-D and QG turbulence, with the major difference of a strong cyclone-anticyclone asymmetry, absent in the barotropic or quasi-geostrophic model, but already found in SW systems. The similarity between the flow considered and QG turbulence is further justified by the horizontal balance diagnostic performed following *Capet et al.* [2008c]. Adopting their relative measure of unbalance (their equation (16)), we find that the mesoscale flow is predominantly in gradient wind balance, with Coriolis plus pressure and advective centrifugal forces dominating the divergence of the horizontal momentum [*McWilliams*, 1985], as in the idealized eastern boundary upwelling current investigated by *Capet et al.* [2008c]. In particular, gradient wind balance is attained in vortex cores, with filamentary regions of ageostrophy at their edges (not shown). If the advective centrifugal forces are neglected, as when the simpler geostrophic balance approximation is used, coherent vortex cores are identified as ageostrophic regions of the flow, because of the curvature effect.

4. Vertical Motion

[16] In this section we show that the geostrophic approximation, while able to capture many of the horizontal transport and mixing properties of the flow field, cannot describe the complex structure of the vertical velocities within and around the vortices.

[17] We first concentrate on the analysis of the daily averaged vertical velocity field, in which the near-inertial component is removed by the time averaging. In the vertical sections across vortices (Figure 6a), upwelling and downwelling regions alternate. High values of vertical velocities, up to 50 m d^{-1}, are found in the proximity of the vortices and are related in a complex way to the vorticity field. Similar patterns and values have been reported in simulations of ocean fronts [*Mahadevan*, 2006], where subsurface intensification is attributed to submesoscale dynamics. In keeping with the instability analysis of *Molemaker and McWilliams* [2005], we infer that in our integrations coherent vortices are regions where anticyclonic ageostrophic instability (AAI) and centrifugal instability may occur. Indeed, strong geostrophic flows (the vortices) and strong, appreciably ageostrophic, vertical motions are colocated. The background turbulence

can be subject to only (geostrophic) baroclinic instability. The submesoscale activity is therefore similar to the one at ocean fronts for the presence of AAI. Here, however, local intensification of lateral buoyancy gradients due to frontogenesis is not present, because of the lack of an imposed lateral velocity shear. In our runs the spatial heterogeneities induced by the wind forcing on the (initially uniform) density field are unable to self-sustain the generation of submesoscale fronts.

[18] The vertical velocity field, w, does not display any evident correlation with the vorticity field or its derivatives. This can be understood by calculating w diagnostically from the flow divergence (see Appendix A for derivation):

$$
\begin{aligned}
w(x,y,z) = \quad & \overset{\text{FREE SURFACE}}{\frac{D\eta}{Dt}} \\[4pt]
& \overset{\text{AGEOSTROPHIC} - \text{AG}}{} \\
& - \int_z^\eta \alpha_1 \left[\frac{\partial \zeta_1}{\partial t} + u \frac{\partial \zeta_1}{\partial x} + v \frac{\partial \zeta_1}{\partial y} + w \frac{\partial \zeta_1}{\partial z} \right] dz \\
& - \int_z^\eta \alpha_2 \left[\frac{\partial \zeta_2}{\partial t} + u \frac{\partial \zeta_2}{\partial x} + v \frac{\partial \zeta_2}{\partial y} + w \frac{\partial \zeta_2}{\partial z} \right] dz \\[4pt]
& \overset{\text{STRETCHING} - \text{ST}}{} \\
& - \int_z^\eta \alpha_1 [\chi_2 \zeta_1] \, dz - \int_z^\eta \alpha_2 [\chi_1 \zeta_2] \, dz \\[4pt]
& \overset{\text{TILTING} - \text{TI}}{} \\
& - \int_z^\eta \alpha_1 \left[\frac{\partial w}{\partial x} \frac{\partial v}{\partial z} \right] dz + \int_z^\eta \alpha_2 \left[\frac{\partial w}{\partial y} \frac{\partial u}{\partial z} \right] dz \\[4pt]
& \overset{\text{WIND STRESS} - \text{EK}}{} \\
& + \int_z^\eta \frac{\alpha_2}{\rho_o} \left[-\frac{\partial}{\partial y} \frac{\partial \tau_x}{\partial z} \right] dz \\[4pt]
& \overset{\text{HORIZONTAL MIXING} - \text{HM}}{} \\
& + \sum_{i=1,2} \int_z^\eta \alpha_i A_H \left(\frac{\partial^4 \zeta_i}{\partial x^4} + \frac{\partial^4 \zeta_i}{\partial y^4} \right) dz \\[4pt]
& \overset{\text{VERTICAL MIXING} - \text{VM}}{} \\
& + \int_z^\eta \alpha_1 \frac{\partial}{\partial x} \frac{\partial}{\partial z} \left(K_v \frac{\partial v}{\partial z} \right) dz - \int_z^\eta \alpha_2 \frac{\partial}{\partial y} \frac{\partial}{\partial z} \left(K_v \frac{\partial u}{\partial z} \right) dz,
\end{aligned}
\tag{1}
$$

where $\zeta_1 = \partial v / \partial x$; $\zeta_2 = -\partial u / \partial y$; $\chi_1 = \partial u / \partial x$; $\chi_2 = \partial v / \partial y$; $\alpha_1 = (f + \zeta_1)^{-1}$; and $\alpha_2 = (f + \zeta_2)^{-1}$.

[19] One day averaged vertical profiles of each of the contributions above are shown in Figure 4a. The primary balance is attained by the nonlinear ageostrophic and stretching terms (of the order of 60 m d^{-1}), which appear in the form of azimuthal wave number $k_A = 4$ disturbances around the vortex cores (Figures 4b and 4c). Those contributions are strongly anticorrelated and largely cancel each other. The cancelation results from the tendency of the vortices to be axisymmetric and to satisfy the gradient wind balance equation (section 2 and *Capet et al.* [2008b]). As a result of this cancelation, the tilting term in the shape of a spiraling wave number $k_A = 2$ band dominates the overall pattern of the vertical velocity field (compares Figures 4d and 2e), reaching values of 20 m d^{-1} at the surface and declining with depth. Vertical mixing contributes up to 10 m d^{-1} close to the surface; free surface, wind stress curl and horizontal mixing terms are smaller by three to 4 orders of magnitude, depending on depth. All terms are modulated by $(f + \zeta)^{-1}$, which can be large inside anticyclones where $|\zeta| \sim f$ and ageostrophic effects arise, generating the fine-scale structure in Figures 2e and 2f and explaining the absence of simple correlations between w and ζ or its spatial gradients. The complexity of the vertical velocity field in the first 100 m is
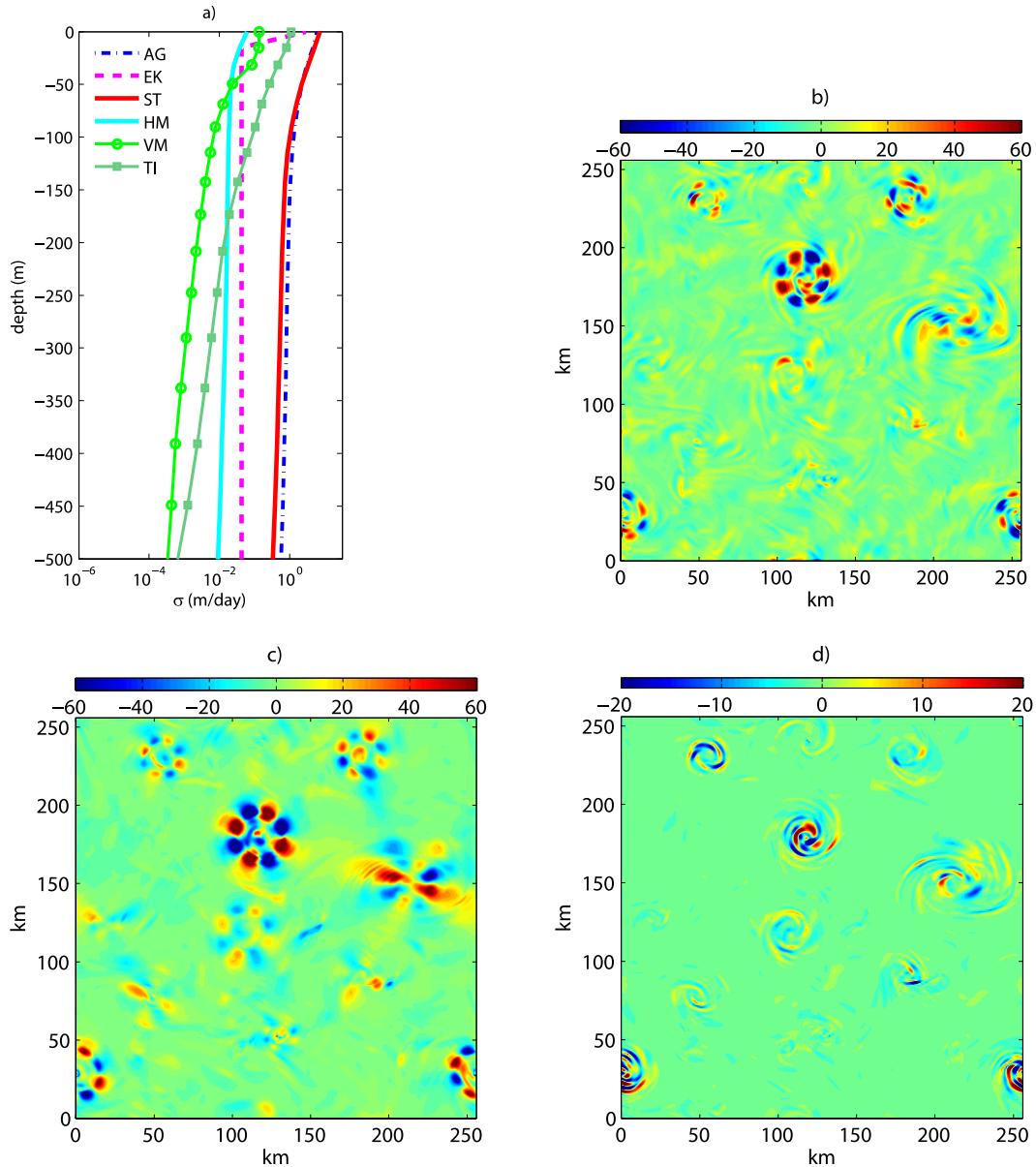
Figure 4. (a) Vertical profile for each of the terms contributing to the vertical velocity in equation (1). All terms have been averaged over 1 day, thus removing near-inertial contributions. (b) Ageostrophic, (c) stretching, and (d) tilting contributions to the vertical velocity field in m d^{-1} at 15 m depth and averaged over 1 day. AG, ageostrophic; EK, Ekman; ST, stretching; HM, horizontal mixing; VM, vertical mixing; TI, tilting.

dominated by low-frequency processes (longer than 1 day) in the form of bands described in previous works as outward propagating vortex Rossby waves (VRWs) [*Montgomery and Kallenbach*, 1997; *McWilliams et al.*, 2003; *Graves et al.*, 2006]. In the paper by *Montgomery and Kallenbach* [1997] VRWs have been identified estimating the local dispersion relation

$$\nu = \frac{k_A \partial_r \zeta}{k_A^2 + k_r^2} \qquad (2)$$

for a spectrally localized wave packet with azimuthal wave number $k_A = 2$, which prevails in the vertical velocity field

of the vortices because of the tilting term. Here the radial wave number is $k_r = 2\pi/\lambda$, where $\lambda \approx 10-15$ km is the typical wavelength of the velocity disturbances for the simulated vortex field and $\partial_r \zeta$ is the differentiation with respect to the radius of the vortex. The frequency varies between $0.15f \leq \nu \leq 0.2f$, which corresponds to a period of $3.6 \leq T_{VRW} \leq 4.8$ days. To our knowledge, this is the first time that vortex Rossby waves have been identified and analyzed in a fully nonlinear regime of oceanic interest using a PE model. Because of the contributions of the ageostrophic terms, VRWs in our solutions differ significantly from the ones occurring in QG flows. VRWs have been extensively studied in the context of tropical cyclogenesis and hurricane intensification [*Montgomery and*
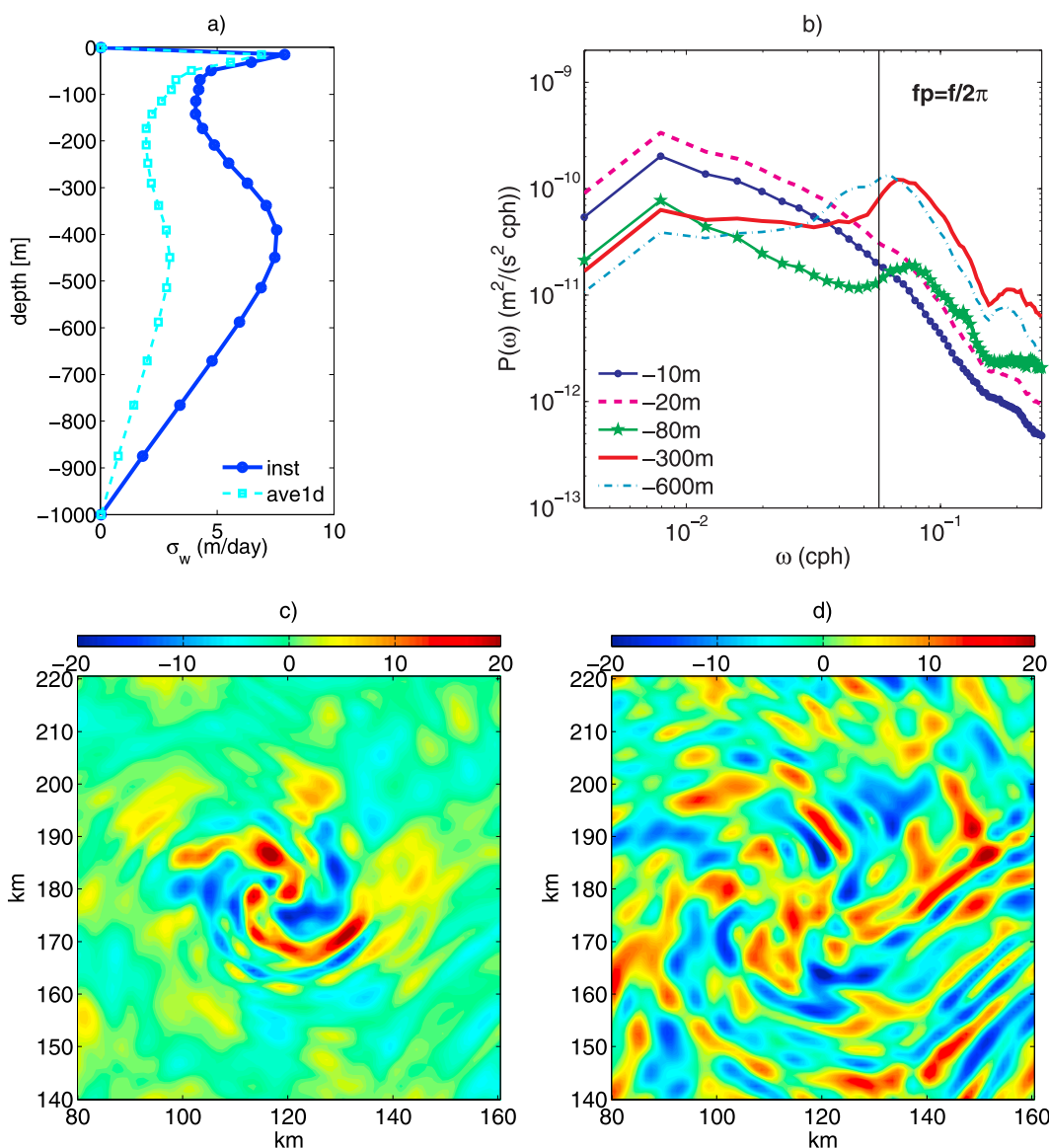
Figure 5. (a) Domain averaged vertical profile of the RMS fluctuation (standard deviation) of the instantaneous vertical velocity field (solid line with circles) and of daily averaged vertical velocity (dashed line with squares). (b) Frequency spectra of vertical velocity at 10, 20, 80, 300, and 600 m, calculated over 10 days at regularly distributed 64×64 points in the domain, using a time step of 2 h. The signal has been linearly detrended. The inertial frequency (fp) is indicated by the black line. Instantaneous snapshot of vertical velocity (in m d^{-1}) (c) at 78 and (d) at 350 m depth in and around the vortex centered at 120 km, 180 km. Snapshots and the instantaneous profile are taken at middle of the day interval over which the daily averaged fields were calculated.

Kallenbach, 1997; *Schubert et al.*, 1999; *Wang*, 2002; *Möller and Shapiro*, 2002].

[20] As shown by *Graves et al.* [2006] for a shallow water flow in a weakly nonlinear regime, VRWs are responsible for the asymmetry of the vortex population. The straining deformation that they induce systematically weakens cyclones, while anticyclones with size comparable to the Rossby deformation radius, as in our simulations, strengthen. While the tilting term with its spiraling bands determines the overall shape of the vertical velocity field within and around the vortices, it should be stressed that velocity maxima are

attained in the regions where the ageostrophic and stretching terms do not cancel each other.

[21] We now concentrate on the contribution of the near-inertial component to the vertical velocity field. Figure 5a shows the vertical profile of the standard deviation of the instantaneous vertical velocity field averaged over the horizontal domain together with the one obtained for the daily averaged vertical velocity field. The maximum that appears at middepth between 300 and 500 m, and that is not pronounced in the 1 day averaged profile, reflects the contribution of near-inertial internal waves to the vertical
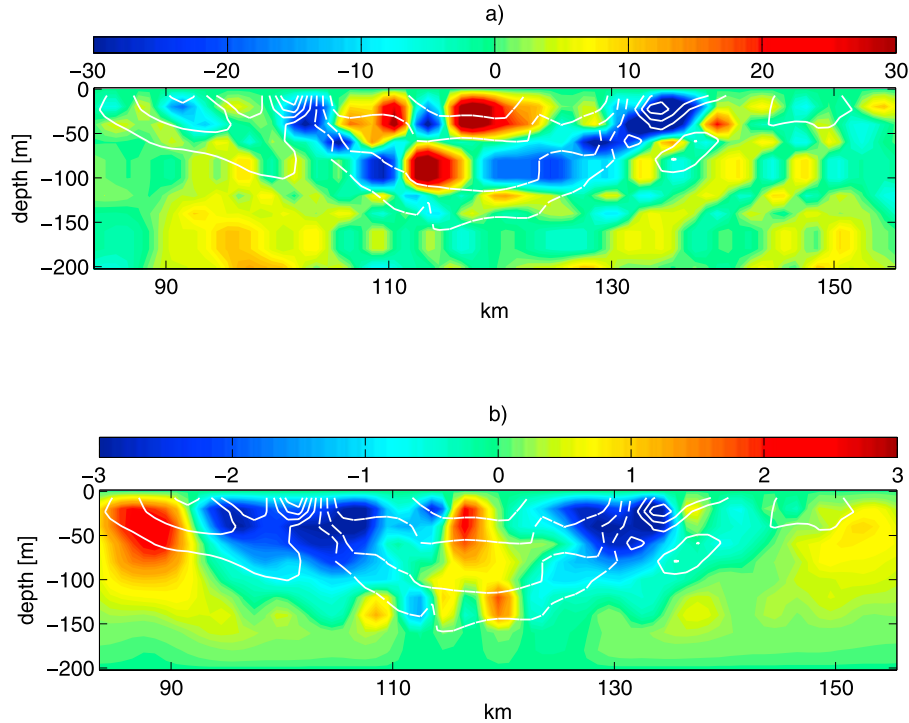
Figure 6. (a) Instantaneous vertical section of vertical velocity (in m d^{-1}) across the line indicated in Figure 2a over the first 200 m of the water column. (b) As in Figure 6a, but obtained from the QG omega equation. The level of no motion is set to 180 m. Note the order of magnitude difference in the amplitude of the signal.

velocity field, as evident in the frequency spectra shown in Figure 5b. The shift of the inertial peak toward a frequency higher than predicted for quasi-geostrophic flows [*Kunze*, 1985] is likely due to the near-inertial motions induced by the ageostrophic instabilities in the vortex cores [*Boccaletti et al.*, 2007] and has been found also in observational data [*Pollard*, 1980; *Millot and Crepon*, 1981; *Kundu and Thomson*, 1985]. Internal gravity waves have negligible amplitude close to the surface compared to the balanced motions (compare Figures 5c and 2e); they have comparable spectral amplitude between 100 and 250 m of depth; and they dominate the dynamics below 300 m (compare Figures 5d and 2f). Amplitudes as high as the ones reported here have been found in high-resolution ocean general circulation model runs in the presence of wind pulses and have been linked to wind-induced energy in the presence of high-frequency atmospheric forcing [*Danioux et al.*, 2008]. Vertical resolution and the mixed layer do impact the amplitude of the near-inertial component that becomes more pronounced for increasing resolution (Figure 8), and we briefly discuss such a dependance at the end of this section.

[22] Further investigating vertical velocities, we examine the accuracy of estimating them using the quasi-geostrophic omega equation. We follow the classical formulation proposed by *Hoskins et al.* [1978] and adopted by, for example, *Pollard and Regier* [1992] and *Pinot et al.* [1996],

$$N^2 \nabla_h^2(w) + f^2 \frac{\partial^2 w}{\partial z^2} = 2\nabla \cdot (Q), \qquad (3)$$

where N is the three-dimensional buoyancy frequency, ∇_h^2 is

$$\nabla_h^2 = \frac{\partial}{\partial x^2} + \frac{\partial}{\partial y^2} \qquad (4)$$

and Q is defined as

$$Q = \frac{g}{\rho_o} \left(\frac{\partial u_g}{\partial x} \frac{\partial \rho}{\partial x} + \frac{\partial v_g}{\partial x} \frac{\partial \rho}{\partial y}, \frac{\partial u_g}{\partial y} \frac{\partial \rho}{\partial x} + \frac{\partial v_g}{\partial y} \frac{\partial \rho}{\partial y} \right). \qquad (5)$$

[23] We solve the QG omega equation using a Fourier transform in horizontal, where periodic boundary conditions are implemented, and a discrete Fourier transform in the vertical, interpolating all the fields required on a 20 m evenly spaced vertical grid. The geostrophic horizontal velocities are calculated from the model pressure field by assuming thermal wind balance. The level of no motion is prescribed at 180 m, the depth at which the influence of the surface-intensified vortices is strongly reduced. Different values, between 125 and 180 m, have been adopted with qualitatively similar results. (We could not test values deeper than 180 m because the stratification profile is exponential and the matrices in the Louville problem become singular). We approximate the free surface as z = 0, and we further apply the rigid lid approximation with w = 0 at z = 0 [*Allen and Smeed*, 1996; *Shearman et al.*, 1999; *Belchi and Tintore*, 2001]. No significant differences are found if the model values of w at z = 0 are used instead, as in the paper by *Pinot et al.* [1996].
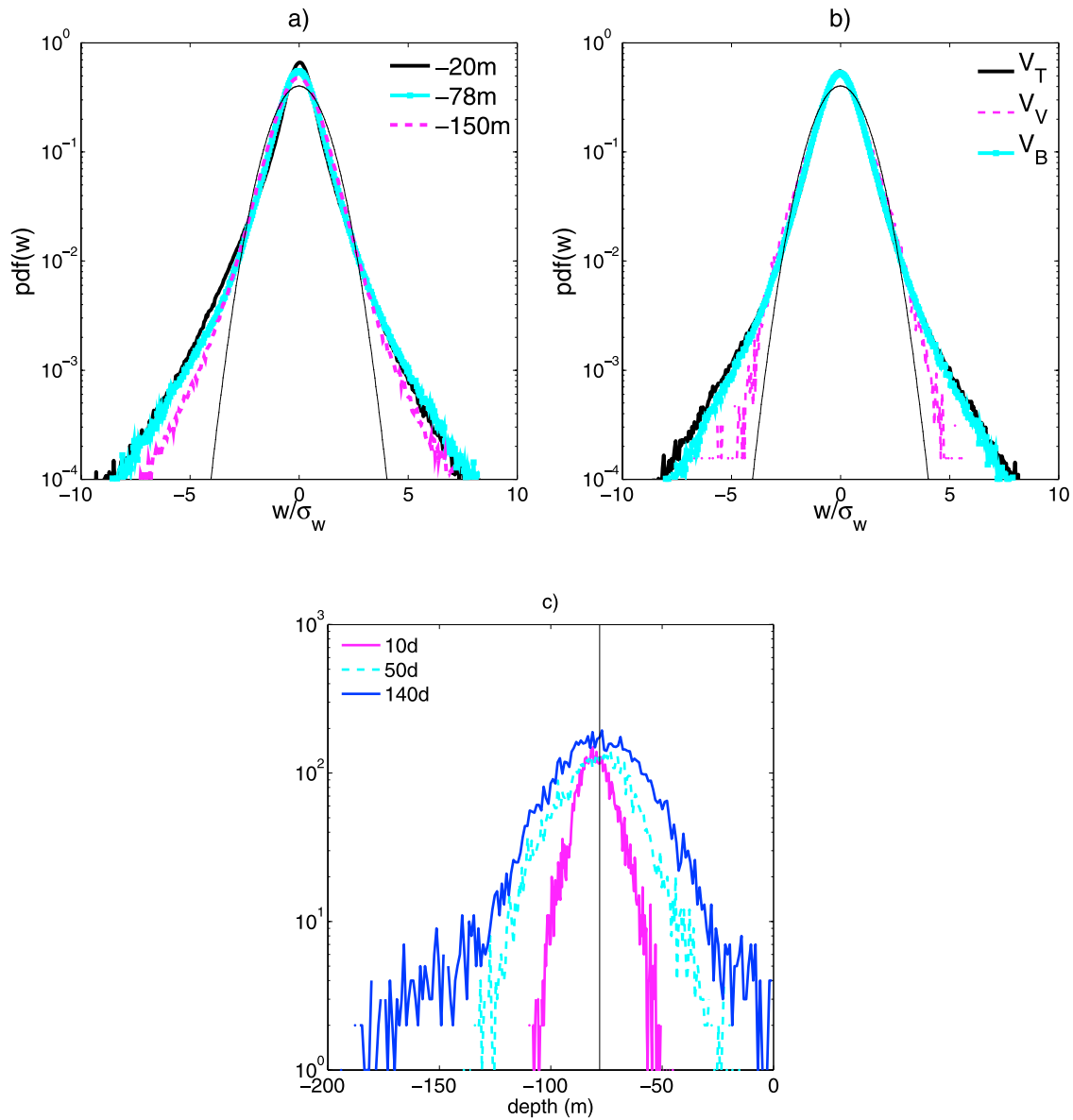
Figure 7. (a) Normalized pdf's of vertical velocities at 20, 78, and 150 m. The thin solid line represents a Gaussian pdf. (b) Normalized pdf's of vertical velocities at 78 m depth inside vortices (V_V), in the background (V_B), and in the whole domain (V_T). The thin solid line represents a Gaussian distribution. The pdf's have been averaged over 50 days during the statistically stationary phase. (c) Histograms of vertical positions of tracers released at 78 m at different times after deployment. The vertical line marks the depth of deployment.

[24] Figure 6a shows the instantaneous vertical section of the vertical velocity field along the white line in Figures 2a–2c (i.e., across the vortex centered at 120 and 180 km) for the model solution and Figure 6b the corresponding field obtained by solving the QG omega equation, together with the isolines of relative vorticity. While the broader features of the vertical velocity field (as the vertical extension and location of the downwelling maxima within the vortex) are somehow captured by the omega equation, the velocity calculated by using equation (3) is 1 order of magnitude weaker in amplitude and smoother than the modeled one. *Pinot et al.* [1996] and *LaCasce and Mahadevan* [2006], among others, also noticed that the

QG omega equation produces patterns of vertical velocity that are too smooth compared to observations.

[25] These results indicate that the vertical velocity estimates provided by the traditional quasi-geostrophic formulations are not a reliable approximation for the vertical transport associated with wind-forced coherent vortices.

[26] Additionally, we find that the distribution of vertical velocities is non-Gaussian in the upper 120 m, where the dynamics is dominated by the presence of the vortices (Figures 7a and 7b), and Gaussian at depth (not shown). Close to the surface the pdf's are slightly skewed toward negative values, as also observed in frontal circulation regions [*Mahadevan*, 2006; *Capet et al.*, 2008c, 2008d]. Vertical velocities significantly impact the vertical trans-
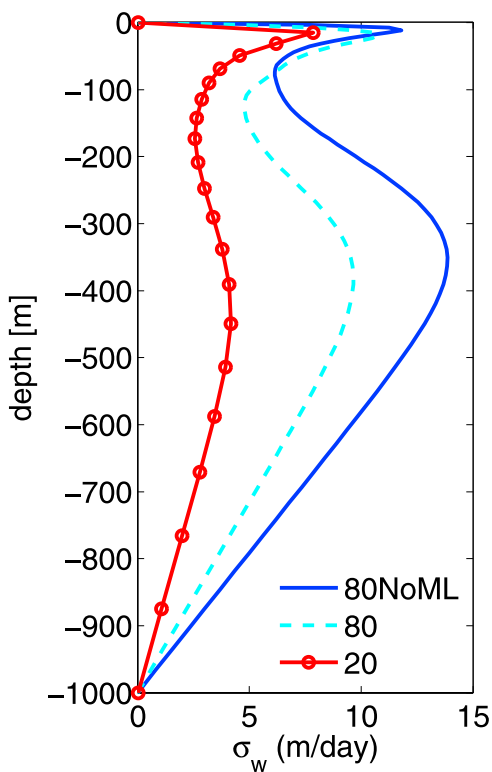
Figure 8. Vertical profile of the instantaneous RMS fluctuation (standard deviation) of vertical velocity averaged over the horizontal domain and 600 snapshots over 50 days in the statistically stationary phase for the 80 layer run with idealized sinusoidal wind forcing in the absence of a mixed layer (solid line), again for the 80 layer run with mixed layer (dashed line), and in the simulation with a narrow-band continuous wind forcing and 20 layer vertical resolution (marked with circles).

port of heat, salt, and any kind of material in the ocean, including plankton. To further study this issue we analyzed the set of homogeneously distributed Lagrangian particle pairs deployed at an initial depth of 78 m. Figure 7c shows the distributions of the vertical positions of the particles at different instants, indicating that passive tracers undergo large vertical excursions. This may have important implications for marine ecosystem dynamics: Assuming in the open ocean the euphotic layer depth is about 70 m, over 50% of the particles released just below the euphotic layer enter it and reach 40 m depth (where the subsurface maximum of phytoplankton concentration is typically located) at least once during any 100 day period, with an average of three visits. The mean duration of each visit is about 10 days, sufficient to make upwelled nutrients available to phytoplankton and potentially trigger a subsurface bloom.

[27] Finally, we compared the simulation described so far with three others where flow has been forced with the idealized sinusoidal wind stress as discussed in section 2. Of those, the first differs from the one considered only in the wind forcing. The second has an increased vertical resolution with 80 layers. The third, also with 80 layers, does not include a mixed layer in the first 20 m of the water column. Horizontal and vertical motion, and transport properties are qualitatively comparable in all runs. The idealized sinusoidal wind stress induces a flow that is also quantitatively similar to the one discussed here. Increasing the vertical resolution from 20 to 80 layers causes the vertical velocities to increase. This is verified in the whole water column, and particularly at middepth, where, for an otherwise identical configuration, the standard deviation is more than twice as large as in the 20 layers case (Figure 8). The general structure of the vertical velocity fields remain, however, similar to what is discussed for the 20 layer case. In the absence of a mixed layer, vertical velocities are further amplified below the surface, because momentum can be transferred more easily from the surface, where only a shallow Ekman layer is formed by the action of the wind forcing, to deeper waters.

5. Discussion and Conclusions

[28] In this work we used the high-resolution PE model ROMS to study an idealized portion of a wind-forced, turbulent open ocean. Differential rotation, topographic, and nonhydrostatic effects have been neglected. As shown by *Mahadevan* [2006], nonhydrostatic terms do not contribute substantially to the average vertical flux on ocean mesoscale.

[29] The results discussed here provide a novel view of the dynamics of vortex-dominated, rotating turbulence in stably stratified fluids. In our integration the internal Rossby deformation radius is small compared to the domain size, resulting in the generation of wind-forced, surface-intensified coherent anticyclones. Cyclones are short living and are destroyed by the straining deformation induced by vortex Rossby waves. In the upper 100 m of the water column, vortical motion dominates over the divergent component; near-inertial waves are negligible; and most statistical properties of horizontal flows, apart from the cyclone-anticyclone asymmetry, are similar to those of 2-D turbulence, with energy spectra slightly steeper than k^{-3}. The vertical velocity field, w, is very complex, and it does not display simple correlations with vorticity or vorticity gradients. Vertical velocities reach high instantaneous values (up to $100 \, \text{m d}^{-1}$) and display a fine spatial structure linked to the presence of vortices and filaments and to their interactions with the Ekman circulation. Within and around vortices and filaments, upwelling and downwelling regions alternate and do not correlate with relative vorticity but result from the interplay of advection, stretching, and instantaneous vorticity changes. Maxima are attained where ageostrophic and stretching terms do not cancel each other, while the overall shape is dominated by the tilting contribution in the shape of a spiraling band. The distribution of vertical velocity is non-Gaussian, and it is responsible for large vertical excursions of Lagrangian tracers. At depth internal gravity waves are responsible for a secondary vertical velocity maximum located, in our runs, between 300 and 400 m.

[30] Shallower spectra than those detected in this work have been observed in simulations of frontal dynamics [*Mahadevan*, 2006; *Capet et al.*, 2008d] and in some basin-scale simulations without small-scale wind forcing [*Klein et al.*, 2008], where the vertical velocity field has been shown to resemble that of sQG dynamics [*Lapeyre*

and Klein, 2006; *Klein et al.*, 2008]. However, the spatial structure of the vertical velocity field studied here is rather different from that predicted by sQG models, possibly for the more energetic dynamics generated by the wind forcing and for the small value of L_d adopted. The flow analyzed is surface-intensified, but not to the point of being describable by an asymptotic approximation such as sQG. A similar example comes from the analysis of vortex merging reported by *von Hardenberg et al.* [2000]: while flattened QG vortices with small aspect ratio do indeed display some of the properties of sQG vortices, the dynamical properties of the merging events and the process of filament instability are rather different.

[31] Our results suggest that, depending on prevailing conditions, mesoscale and submesoscale ocean flows can display different dynamics, from strong frontal development [*Mahadevan*, 2006] to sQG-like flows [*Klein et al.*, 2008] to almost 2-D coherent vortices with complex vertical velocities, as observed here. Further studies are clearly needed to define a more complete regime diagram in parameter space.

Appendix A

[32] Equation (1) has been obtained cross differentiating the horizontal momentum equations integrated by ROMS according to

$$\frac{\partial}{\partial y}\left[\frac{Du}{Dt} - fv = \frac{1}{\rho_o}\frac{\partial \tau_x}{\partial z} + A_H\left(\frac{\partial^4}{\partial x^4} + \frac{\partial^4}{\partial y^4}\right)u + \frac{\partial}{\partial z}\left(K_v\frac{\partial u}{\partial z}\right)\right] \quad (A1)$$

$$\frac{\partial}{\partial x}\left[\frac{Dv}{Dt} + fu = \frac{1}{\rho_o}\frac{\partial \tau_y}{\partial z} + A_H\left(\frac{\partial^4}{\partial x^4} + \frac{\partial^4}{\partial y^4}\right)v + \frac{\partial}{\partial z}\left(K_v\frac{\partial v}{\partial z}\right)\right], \quad (A2)$$

where (u, v) are the horizontal velocity components, $D/Dt = \partial_t + u\partial_x + v\partial_y + w\partial_z$, w is the vertical velocity, and ρ_o is a constant reference density. The formulation includes biharmonic horizontal mixing, with A_H being the constant mixing coefficient, and KPP vertical mixing, with $K_v(x, y, z)$ being the vertical mixing coefficient computed by the KPP scheme.

[33] With a little algebra we obtain

$$-\frac{\partial v}{\partial y}\left(f - \frac{\partial u}{\partial y}\right) = \frac{D(-\partial_y u)}{Dt} + \frac{\partial u}{\partial x}\left(-\frac{\partial u}{\partial y}\right) - \left(\frac{\partial w}{\partial y}\frac{\partial u}{\partial z}\right)$$
$$+ \frac{1}{\rho_o}\left[\frac{\partial}{\partial y}\frac{\partial \tau_x}{\partial z}\right] - A_H\left(\frac{\partial^4}{\partial x^4} + \frac{\partial^4}{\partial y^4}\right)\left(-\frac{\partial u}{\partial y}\right)$$
$$+ \frac{\partial}{\partial y}\frac{\partial}{\partial z}\left(K_v\frac{\partial u}{\partial z}\right) \quad (A3)$$

$$-\frac{\partial u}{\partial x}\left(f + \frac{\partial v}{\partial x}\right) = \frac{D(\partial_x v)}{Dt} + \frac{\partial v}{\partial y}\left(\frac{\partial v}{\partial x}\right) + \left(\frac{\partial w}{\partial x}\frac{\partial v}{\partial z}\right)$$
$$- \frac{1}{\rho_o}\left[\frac{\partial}{\partial x}\frac{\partial \tau_y}{\partial z}\right] - A_H\left(\frac{\partial^4}{\partial x^4} + \frac{\partial^4}{\partial y^4}\right)\left(\frac{\partial v}{\partial x}\right)$$
$$- \frac{\partial}{\partial x}\frac{\partial}{\partial z}\left(K_v\frac{\partial v}{\partial z}\right), \quad (A4)$$

which can be rewritten, by defining $\zeta_1 = \partial v/\partial x$, $\zeta_2 = -\partial u/\partial y$, $\chi_1 = \partial u/\partial x$, $\chi_2 = \partial v/\partial y$, as

$$-\frac{\partial v}{\partial y}(f + \zeta_2) = \left[\frac{D\zeta_2}{Dt} + \chi_1\zeta_2 - \frac{\partial w}{\partial y}\frac{\partial u}{\partial z} + \frac{1}{\rho_o}\frac{\partial}{\partial y}\frac{\partial \tau_x}{\partial z}\right.$$
$$\left. - A_H\left(\frac{\partial^4}{\partial x^4} + \frac{\partial^4}{\partial y^4}\right)\zeta_2 + \frac{\partial}{\partial y}\frac{\partial}{\partial z}\left(K_v\frac{\partial u}{\partial z}\right)\right] \quad (A5)$$

$$-\frac{\partial u}{\partial x}(f + \zeta_1) = \left[\frac{D\zeta_1}{Dt} + \chi_2\zeta_1 + \frac{\partial w}{\partial x}\frac{\partial v}{\partial z} - \frac{1}{\rho_o}\frac{\partial}{\partial x}\frac{\partial \tau_y}{\partial z}\right.$$
$$\left. - A_H\left(\frac{\partial^4}{\partial x^4} + \frac{\partial^4}{\partial y^4}\right)\zeta_1 - \frac{\partial}{\partial x}\frac{\partial}{\partial z}\left(K_v\frac{\partial v}{\partial z}\right)\right]. \quad (A6)$$

[34] Equation (1) is then obtained integrating the expression for $\frac{\partial w}{\partial x} = -\frac{\partial u}{\partial x} - \frac{\partial v}{\partial y}$ that is given by the sum of equation (A5) divided by $(f + \zeta_2)$, with equation (A6) divided by $(f + \zeta_1)$.

[35] Alternatively, by adding equations (A5) and (A6) and subsequently moving the χ terms on the left-hand side, we obtain

$$-\frac{\partial v}{\partial y}(f + \zeta_2) - \frac{\partial u}{\partial x}(f + \zeta_1) - \chi_1\zeta_2 - \chi_2\zeta_1$$
$$= \frac{D\zeta_2}{Dt} + \frac{D\zeta_1}{Dt} + \frac{\partial w}{\partial x}\frac{\partial v}{\partial z} - \frac{\partial w}{\partial y}\frac{\partial u}{\partial z}$$
$$+ \frac{1}{\rho_o}\left(\frac{\partial}{\partial y}\frac{\partial \tau_x}{\partial z} - \frac{\partial}{\partial x}\frac{\partial \tau_y}{\partial z}\right) - A_H\left(\frac{\partial^4}{\partial x^4} + \frac{\partial^4}{\partial y^4}\right)(\zeta_1 + \zeta_2)$$
$$+ \frac{\partial}{\partial y}\frac{\partial}{\partial z}\left(K_v\frac{\partial u}{\partial z}\right) - \frac{\partial}{\partial x}\frac{\partial}{\partial z}\left(K_v\frac{\partial v}{\partial z}\right). \quad (A7)$$

Being $-\frac{\partial v}{\partial y}(f + \zeta_2) - \frac{\partial u}{\partial x}(f + \zeta_1) - \chi_1\zeta_2 - \chi_2\zeta_1 = (f + \zeta_1 + \zeta_2)(-\frac{\partial u}{\partial x} - \frac{\partial v}{\partial y}) = (f + \zeta)\frac{\partial w}{\partial z}$, the resulting expression for $\frac{\partial w}{\partial z}$ is directly related to the vorticity equation in the Boussinesq approximation [e.g., *Vallis*, 2006, chapter 4],

$$\frac{\partial w}{\partial z} = \frac{1}{(f + \zeta)}\left[\frac{D\zeta}{Dt} + \frac{\partial w}{\partial x}\frac{\partial v}{\partial z} - \frac{\partial w}{\partial y}\frac{\partial u}{\partial z} + \frac{1}{\rho_o}\left(\frac{\partial}{\partial y}\frac{\partial \tau_x}{\partial z} - \frac{\partial}{\partial x}\frac{\partial \tau_y}{\partial z}\right)\right.$$
$$\left. - A_H\left(\frac{\partial^4}{\partial x^4} + \frac{\partial^4}{\partial y^4}\right)\zeta + \frac{\partial}{\partial y}\frac{\partial}{\partial z}\left(K_v\frac{\partial u}{\partial z}\right) - \frac{\partial}{\partial x}\frac{\partial}{\partial z}\left(K_v\frac{\partial v}{\partial z}\right)\right]. \quad (A8)$$

[36] In this work, the chosen formulation allows for highlighting the azimuthal wave number $k_A = 4$ Rossby waves that largely balance in the interplay between the ageostrophic and stretching terms of equation (1).

References

Allen, J. T., and D. A. Smeed (1996), Potential vorticity and vertical velocity at the Iceland-Faeroes Front, *J. Phys. Oceanogr.*, 26, 2611–2634.

Arai, M., and T. Yamagata (1994), Asymmetric evolution of eddies in rotating shallow water, *Chaos*, 4, 163–173.

Babiano, A., and A. Provenzale (2007), Coherent vortices and tracer cascades in two-dimensional turbulence, *J. Fluid Mech.*, *574*, 429–448.

Babiano, A., C. Basdevant, B. Legras, and R. Sadourny (1987), Vorticity and passive-scalar dynamics in two-dimensional turbulence, *J. Fluid Mech.*, *197*, 241–257.

Babiano, A., C. Basdevant, P. Roy, and R. Sadourny (1990), Relative dispersion in two-dimensional turbulence, *J. Fluid Mech.*, *214*, 535–557.

Belchi, P.-V., and J. Tintore (2001), Vertical velocities at an ocean front, *Sci. Mar.*, *65*(1), 291–300.

Berloff, P., J. C. McWilliams, and A. Bracco (2002), Material transport in oceanic gyres. Part I: Phenomenology, *J. Phys. Oceanogr.*, *32*, 764–796.

Berloff, P., S. Kravtsov, W. Dewar, and J. McWilliams (2007), Ocean eddy dynamics in a coupled ocean-atmosphere model, *J. Phys. Oceanogr.*, *37*, 1103–1121.

Boccaletti, G., R. Ferrari, and B. Fox-Kemper (2007), Mixed layer instabilities and restratification, *J. Phys. Oceanogr.*, *37*, 2228–2250.

Bracco, A., J. H. LaCasce, C. Pasquero, and A. Provenzale (2000a), The velocity distribution of barotropic turbulence, *Phys. Fluids*, *12*, 2478–2488.

Bracco, A., J. H. LaCasce, and A. Provenzale (2000b), Velocity probability density functions for oceanic floats, *J. Phys. Oceanogr.*, *30*, 461–474.

Bracco, A., J. von Hardenberg, A. Provenzale, J. B. Weiss, and J. C. McWilliams (2004), Dispersion and mixing in quasigeostrophic turbulence, *Phys. Rev. Lett.*, *92*, 1–4.

Capet, X., P. Klein, B. L. Hua, G. Lapeyre, and J. C. McWilliams (2008a), Surface kinetic and potential energy transfer in SQG dynamics, *J. Fluid Mech.*, *604*, 165–175.

Capet, X., J. C. McWilliams, M. J. Molemaker, and A. F. Shchepetkin (2008b), Mesoscale to submesoscale transition in the California Current System. Part I: Flow structure, eddy flux and observational tests, *J. Phys. Oceanogr.*, *38*, 29–43.

Capet, X., J. C. McWilliams, M. J. Molemaker, and A. F. Shchepetkin (2008c), Mesoscale to submesoscale transition in the California Current System. Part II: Frontal processes, *J. Phys. Oceanogr.*, *38*, 44–64.

Capet, X., J. C. McWilliams, M. J. Molemaker, and A. F. Shchepetkin (2008d), Mesoscale to submesoscale transition in the California Current System. Part III: Energy balance and flux, *J. Phys. Oceanogr.*, *38*, 2256–2269.

Cho, J., and L. M. Polvani (1996), The emergence of jets and vortices in freely evolving, shallow-water turbulence on a sphere, *Phys. Fluids*, *8*, 1531–1552.

Conkright, M. E., R. A. Locarnini, H. E. Garcia, T. D. O'Brien, T. Boyer, C. Stephens, and J. I. Antonov (2002), *World Ocean Atlas 2001: Objective Analyses, Data Statistics, and Figures* [CD-ROM], edited by D. L. Evans, C. C. Lautenbacher, and G. W. Withee, *NODC Internal Rep. 17*, Ocean Clim. Lab., Natl. Oceanogr. Data Cent., Silver Spring, Md. (Available at http://www.nodc.noaa.gov/OC5/WOA01/woa01dat.html.)

Constantin, P., Q. Nie, and N. Schorghofer (1999), Front formation in an active scalar equation, *Phys. Rev. E*, *60*, 2858–2863.

Cushman-Roisin, B., and B. Tang (1990), Geostrophic turbulence and emergence of eddies beyond the radius of deformation, *J. Phys. Oceanogr.*, *20*, 97–113.

Danioux, E., P. Klein, and P. Reviére (2008), Propagation of wind energy into the deep ocean through a fully turbulent mesoscale eddy field, *J. Phys. Oceanogr.*, *38*, 2224–2241.

Elhmaidi, D., A. Provenzale, and A. Babiano (1993), Elementary topology of two-dimensional turbulence from a Lagrangian viewpoint and single-particle dispersion, *J. Fluid Mech.*, *257*, 533–558.

Graves, L. P., J. C. McWilliams, and M. T. Montgomery (2006), Vortex evolution due to straining: A mechanism for dominance of strong, interior anticyclones, *Geophys. Astrophys. Fluid Dyn.*, *100*, 151–183.

Held, I., R. Pierrehumbert, S. Garner, and K. Swanson (1995), Surface quasi-geostrophic dynamics, *J. Fluid Mech.*, *282*, 1–20.

Hogg, A., P. D. Killworth, J. R. Blundell, and W. K. Dewar (2005), On the mechanisms of decadal variability of the wind-driven ocean circulation, *J. Phys. Oceanogr.*, *35*, 512–531.

Hoskins, B. J., I. Draghici, and H. C. Davies (1978), A new look at the ω-equation, *Q. J. R. Meteorol. Soc.*, *104*, 31–38.

Isern-Fontanet, J., E. Garcia-Ladona, J. Font, and A. Garcia-Olivares (2006), Non-Gaussian velocity probability density functions: An altimetric perspective of the Mediterranean Sea, *J. Phys. Oceanogr.*, *36*, 2153–2164.

Klein, P., L. Hua, G. Lapeyre, X. Capet, S. L. Gentil, and H. Sasaki (2008), Upper ocean turbulence from high-resolution 3D simulations, *J. Phys. Oceanogr.*, *38*, 1748–1763.

Kundu, P. K., and R. E. Thomson (1985), Inertial oscillations due to a moving front, *J. Phys. Oceanogr.*, *15*, 1076–1084.

Kunze, E. (1985), Near-inertial wave propagation in geostrophic shear, *J. Phys. Oceanogr.*, *15*, 544–565.

LaCasce, J. H. (2005), On the Eulerian and Lagrangian velocity distributions in the North Atlantic, *J. Phys. Oceanogr.*, *35*, 2327–2336.

LaCasce, J. H., and A. Mahadevan (2006), Estimating subsurface horizontal and vertical velocities from sea-surface temperature, *J. Mar. Res.*, *64*, 695–721.

LaCasce, J. H., and C. Ohlmann (2003), Relative dispersion at the surface of the Gulf of Mexico, *J. Mar. Res.*, *61*, 285–312.

Lapeyre, G., and P. Klein (2006), Dynamics of the upper oceanic layers in terms of surface quasigeostrophic theory, *J. Phys. Oceanogr.*, *36*, 165–176.

Large, W. G., J. C. McWilliams, and S. Doney (1994), Oceanic vertical mixing: A review and a model with a nonlocal K-profile boundary layer parameterization, *Rev. Geophys.*, *32*, 363–403.

Levy, M., and P. Klein (2004), Does the low frequency variability of mesoscale dynamics explain a part of the phytoplankton and zooplankton spectral variability?, *Proc. R. Soc. London, Ser. A*, *460*, 1673–1687.

Levy, M., P. Klein, and A.-M. Treguier (2001), Impact of sub-mesoscale physics on production and subduction of phytoplankton in an oligotrophic regime, *J. Mar. Res.*, *59*, 535–565.

Mahadevan, A. (2006), Modelling vertical motion at ocean fronts: Are nonhydrostatic effects relevant at mesoscales?, *Ocean Dyn.*, *14*, 222–240.

Mahadevan, A., and A. Tandon (2006), An analysis of mechanisms for submesoscale vertical motion at ocean fronts, *Ocean Dyn.*, *14*, 241–256.

McWilliams, J. C. (1984), The emergence of isolated coherent vortices in turbulent flow, *J. Fluid Mech.*, *146*, 21–43.

McWilliams, J. C. (1985), Submesoscale, coherent vortices in the ocean, *Rev. Geophys.*, *23*, 165–182.

McWilliams, J. C. (1990), The vortices of two-dimensional turbulence, *J. Fluid Mech.*, *219*, 361–385.

McWilliams, J. C., J. B. Weiss, and I. Yavneh (1994), Anisotropy and coherent vortex structures in planetary turbulence, *Science*, *264*, 410–413.

McWilliams, J. C., L. P. Graves, and M. T. Montgomery (2003), A formal theory for vortex Rossby waves and vortex evolution, *Geophys. Astrophys. Fluid Dyn.*, *97*, 275–309.

Millot, C., and M. Crepon (1981), Inertial oscillations on the continental shelf of the Gulf of Lions — Observations and theory, *J. Phys. Oceanogr.*, *11*, 639–657.

Molemaker, M. J., and J. C. McWilliams (2005), Baroclinic instability and loss of balance, *J. Phys. Oceanogr.*, *35*, 1505–1517.

Möller, J. D., and L. J. Shapiro (2002), Balanced contributions to the intensification of Hurricane Opal as diagnosed from a GFDL model forecast, *Mon. Weather Rev.*, *130*, 1866–1881.

Montgomery, M. T., and R. K. Kallenbach (1997), A theory for vortex Rossby waves and its application to spiral bands and intensity changes in hurricanes, *Q. J. R. Meteorol. Soc.*, *123*, 435–465.

Pasquero, C., A. Provenzale, and A. Babiano (2001), Parameterization of dispersion in two-dimensional turbulence, *J. Fluid Mech.*, *439*, 279–303.

Petersen, M. R., K. Julien, and J. B. Weiss (2006), Vortex cores, strain cells, and filaments in quasigeostrophic turbulence, *Phys. Fluids*, *18*, 1–11.

Pinot, J.-M., J. Tintore, and D.-P. Wang (1996), A study of the omega equation for diagnosing vertical motions at ocean fronts, *J. Mar. Res.*, *54*, 239–259.

Pollard, R. T. (1980), Properties of near-surface inertial oscillations, *J. Phys. Oceanogr.*, *10*, 385–398.

Pollard, R. T., and L. A. Regier (1992), Vorticity and vertical circulation at an ocean front, *J. Phys. Oceanogr.*, *22*, 609–625.

Polvani, L. M., J. C. McWilliams, M. A. Spall, and R. Ford (1994), The coherent structures of shallow-water turbulence: Deformation radius effects, cyclone/anticyclone asymmetry and gravity-wave generation, *Chaos*, *4*, 177–186.

Provenzale, A. (1999), Transport by coherent barotropic vortices, *Annu. Rev. Fluid Mech.*, *31*, 55–93.

Richardson, L. F. (1926), Atmospheric diffusion shown on a distance-neighbor graph, *Proc. R. Soc. London, Ser. A*, *110*, 709–737.

Schorghofer, N. (2000), Universality of probability distributions among two-dimensional turbulent flows, *Phys. Rev. E*, *61*, 6568–6571.

Schubert, W. H., M. T. Montgomery, R. K. Taft, T. A. Guinn, S. R. Fulton, J. P. Kossin, and J. P. Edwards (1999), Polygonal eyewalls, asymmetric eye contraction, and potential vorticity mixing in hurricanes, *J. Atmos. Sci.*, *56*, 1197–1223.

Shchepetkin, A., and J. C. McWilliams (1998), Quasi-monotone advection schemes based on explicit locally adaptive dissipation, *Mon. Weather Rev.*, *126*, 1541–1580.

Shchepetkin, A., and J. C. McWilliams (2005), The Regional Oceanic Modelling System (ROMS): A split-explicit, free-surface, topography-following-coordinate oceanic model, *Ocean Dyn.*, *9*, 347–404.

Shearman, R. K., J. A. Barth, and P. M. Kosro (1999), Diagnosis of the three-dimensional circulation associated with mesoscale motion in the California Current, *J. Phys. Oceanogr.*, *29*, 651–670.

Smith, K. S., and G. K. Vallis (2001), The scales and equilibration of midocean eddies: Freely evolving flow, *J. Phys. Oceanogr.*, *31*, 554–571.

Smith, K. S., and G. K. Vallis (2002), The scales and equilibration of midocean eddies: Forced-dissipative flow, *J. Phys. Oceanogr.*, *32*, 1699–1720.

Stammer, D. (1997), Global characteristics of ocean variability estimated from regional TOPEX/POSEIDON altimeter measurements, *J. Phys. Oceanogr.*, *27*, 1743–1769.

Vallis, G. (2006), *Atmospheric and Oceanic Fluid Dynamics*, Cambridge Univ. Press, New York.

von Hardenberg, J., J. C. McWilliams, A. Provenzale, A. Shchepetkin, and J. B. Weiss (2000), Vortex merging in quasi-geostrophic flows, *J. Fluid Mech.*, *412*, 331–353.

Wang, Y. (2002), Vortex Rossby waves in a numerically simulated tropical cyclone. Part I: Overall structure, potential vorticity, and kinetic energy budgets, *J. Atmos. Sci.*, *59*, 1213–1238.

Weiss, J. (1981), The dynamics of enstrophy transfer in two-dimensional turbulence, *Physica D*, *48*, 273–294.

Yavneh, I., A. F. Shchepetkin, J. C. McWilliams, and L. P. Graves (1997), Multigrid solutions of rotating, stably stratified flows: The balance equations and their turbulent dynamics, *J. Comput. Phys.*, *136*, 245–262.

————————————

A. Bracco, School of Earth and Atmospheric Science, Georgia Institute of Technology, Atlanta, GA 30332, USA. (abracco@gatech.edu)

I. Koszalka, Institute of Geosciences, University of Oslo, 1022 Blindern, N-0315 Oslo, Norway.

J. C. McWilliams, Institute of Geophysics and Planetary Physics, University of California, Los Angeles, CA 90095-1565, USA. (jcm@atmos.ucla.edu)

A. Provenzale, ISAC, CNR, Torino, I-10100, Italy.